

CFD and Experimental Investigations of Drag Force on Spherical Leak Detector in Pipe Flows at High Reynolds Number

ShiXu Guo¹, Shili Chen¹, Xinjing Huang¹, Yu Zhang¹ and Shijiu Jin¹

Abstract: Spherical leak detectors can detect very tiny leakage in pipelines and have low risk of blockage. In this paper the passing ability of the detector in the vertical segment of a pipe was studied using CFD simulations and experiments. The Reynolds number for the sphere exceeds 10^4 at the economical velocity range for oil pipelines, and there were few researches related to the hydrodynamic force on the sphere by the pipe flow at high Reynolds number. For sphere with different sizes and density, and at different flow rates, more than 100 3-D steady numerical simulations were carried out. The simulation data was verified by comparing the experimental critical velocity with that of the simulation, the results shows that they agree well with each other. The drag on the sphere is related to the flow velocity V and the diameter ratio λ . The effect of flow velocity was more significant at $\lambda > 0.65$. An empirical formula for the drag with λ and V is established for $0.2 \leq \lambda \leq 0.9$, $4000 \leq Re_s \leq 54000$. The passing ability of the sample detector in 8-28 inch pipelines is predicted; it shows that the detector could go through the vertical pipe under normal economical flow velocity (0.7m/s-1.5m/s) in 8 or 10-inch pipelines. A passing ability test of the sample detector was carried out in an 8-inch pipe loop The optimal range for λ (0.7~0.8) is given based on the analysis results.

Keywords: spherical leak detector, passing ability, vertical pipeline, CFD computation, diameter ratio.

1 Introduction

As the main method for offshore oil and gas transportation, submarine pipelines have become the development and transportation lifeline for marine oil and gas resources. Due to the instability of the seabed foundation, medium corrosion, ocean

¹ State Key Laboratory of Precision Measurement Technology and Instrument, Tianjin University, Tianjin, China.

current scouring and offshore operations, leakage accidents of submarine oil and gas pipeline occur frequently. This results in a huge economic loss and marine environmental pollution. In order to eliminate potential security risks in pipeline operation and avoid leak accidents, timely measures must be taken to detect and locate subtle leakage in these pipelines. The present leak detecting methods for pipelines can be divided into two broad categories: internal detection and external detection. The latter, includes methods such as negative pressure wave [Tian, Yan, Huang, Wang, Kim and Yi (2012)], acoustic correlation [Fuchs and Riehle (1991)] and optical fiber leakage method [Zhou and Yin (2012)]. All of these are widely used in land pipelines which are suitable for paroxysmal leakage and can only detect leak rates at 1% of total flow for oil pipelines or 5% in case of gas pipelines. This may not be useful when dealing with leak detection in submarine pipelines because such a large leak already exceeds the criteria of a major accident and would seriously affect the marine environment. A critical need for offshore pipelines is detection technology for small leaks. Internal methods depend on the detector getting close to the leak point inside the pipe to monitor leakage signals. Theoretically, it can detect very small oil and gas leaks.

Traditional internal detectors (PIG, Pipeline Inspection Gauge) move forward driven by the pressure differences between the front and the back of the detectors, and gets information about corrosion, defect and weld conditions on the inner walls of pipeline [Quarini and Shire (2007); Gloria, Areiza, Miranda and Rebello (2009)]. PIG detectors are based on acoustic technology [Lopez and Sadovnychiy (2007); Lei, Huang, Liang, Mao and Que (2009)], such as the GLD leak detection system, where the detector moves with the flow inside the pipe and collects leak noise in the ultrasonic range using a hydrophone mounted on the detector [Bockler (2012)]. It has a great sensitivity for leaks of less than 1 L/min. However, the PIG is bulky and fits closely to the wall of the pipe, which generates lots of noises by the friction between the wheels on the PIG and the wall of the pipe when passing along the pipe, making it difficult to extract the weak leak noise. And the PIG is sensitive to any deformation or bends, causing high-risk of blockage, which limit its further application in offshore pipelines.

Recently, a free-swimming, un-tethered acoustic leak detector called Smartball is being addressed [Li, Chen, Zhao, Guo and Liu (2012); Fletcher and Chandrasekaran (2009)]. The Smartball device diverges from the traditional cylindrical shape of in-line equipment or “pigs”. The spherical shape greatly reduces the noise produced by the device as it passes along the pipe and it is able to negotiate a much wider range of bore changes, small radius bends and other obstacles that may exist within the pipe. It also has a sensitivity of less than 0.1L/min. Due to its high sensitivity and low risk for blockage; this technology is highly suitable for detection of

small leaks in offshore pipelines. Nevertheless, the vertical segment for submarine pipes often is as high as hundreds of meters. Once the detector cannot go through the pipe's vertical segment smoothly, the detection and location sensitivity would be hindered. In addition, normal operation of pipeline would also be affected and could result in a major safety accident. Therefore, it is of critical to investigate the passing ability of spherical inner detector through the vertical segment of the submarine pipeline.

In order to improve the efficiency of oil transportation, the economical velocity usually ranges from 0.49m/s to 2.25m/s in China [Tang (2007)]. So, the Re_s in the pipeline exceeds 10^4 , however, there were little research about the hydrodynamic force on the sphere by the pipe flow and the passing ability of the sphere in vertical segment of the pipe at high Reynolds number for the sphere (Re_s). Hydrodynamic and heat transfer analyses were carried out for laminar fluid flow past a heated sphere placed centrally in a pipe using CFD simulations ($Re_s < 500$, $\lambda < 0.5$) [Krishnan and Kannan (2010)]. The flow and drag phenomena of confined spherical particles in shear-thickening fluids has been investigated using a numerical approach for a range of $Re_s < 100$, $\lambda < 0.5$ [Song, Gupta and Chhabra (2009); Rajasekhar Reddy and Kishore (2012)]. Six different Re_s ranging from 0.1 to 1 and seven different diameter ratios λ ranging from 0.025 to 0.2 were selected to study the pipe-wall effect [Lee and Wu (2007)].

A nonporous sphere of diameter d driven by an infinite Newtonian fluid of dynamic viscosity μ and density ρ at an average velocity of V experiences hydrodynamic force of F_t , which can be expressed as:

$$F_t = \left(\frac{\pi d^2}{4} \right) \left(\frac{1}{2} \rho V^2 \right) C_D \quad (1)$$

where C_D denotes the drag coefficient. For conditions when Stokes law is applicable (Reynolds number for the sphere Re_s is less than unity), then $C_D = 24/Re_s$

Reynolds number for the sphere:

$$Re_s = \frac{dV\rho}{\mu} \quad (2)$$

Reynolds number for the pipe:

$$Re_p = \frac{DV\rho}{\mu} \quad (3)$$

Diameter ratio:

$$\lambda = \frac{d}{D} \quad (4)$$

Oil and gas pipelines are finite boundaries and the Stokes law may not be justifiable. The role of wall effects on the rolling velocity of sphere in Newtonian fluids have been studied and were found to have a very limited correlation for $\lambda > 0.707$ and $Re_s < 2100$ and the drag coefficient can then be expressed as [Hasan (1986)]:

$$C_D = \frac{15.717}{Re_s} \left(1 - \left(\frac{d}{D} \right) \right)^{-2.5} \quad (5)$$

A valuable experimental work for drag on spheres in rolling motion in inclined smooth tubes has been investigated. Based on this study they defined an empirical correlation using 900 data points. And the drag coefficient can then be expressed as: [Jalaal and Ganji (2011); Chhabra, Kumar and Prasad (2000)]:

$$C_D = 1.2 + \frac{190}{Re_s} + \frac{1.003 \times 10^{-7}}{Re_s^2} \quad (6)$$

The Reynolds number range was $10^{-6} < Re_s < 3000$ and the $\lambda < 0.5$. It was concluded that the diameter ratio λ is not a significant parameter at 95% confidence level.

It is not necessary and economical to build loops in series using real pipes to study this problem. A miniature model was built to study the passing ability of the spherical leak detector inside the vertical segment of the pipe. Both simulation and experiment methods are used in this paper. In this paper, the methods used for numerical simulation and the experiments are first introduced. After which, the pressure and flow behavior around the sphere and inside the pipe with different λ and V are analyzed. The drag on the sphere is calculated and an empirical formula for the total drag with λ and V is established. Finally, the simulation and experimental data are compared and the passing ability of the prototype spherical leak detector in the real pipeline is analyzed and verified at a 150m long and diameter of 200mm pipe loop.

2 Numerical simulation and experimental methods

2.1 Problem statement and governing equations

Take the sphere along the central axis of the vertical pipe as research object, as shown schematically in Fig.1. Under ideal conditions, it is only subject to three forces, i.e. F_f , F_t and G , where, F_t is the vertical upward drag, caused by the fluid pressure and fluid velocity energy; F_t and G are the buoyancy and gravity respectively. It is assume here that the sphere is stationary and is solved here for the critical state. The total vertical force is as follows:

$$F_h = F_t + F_f - G \quad (7)$$

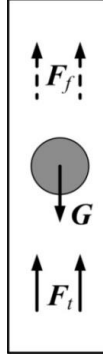


Figure 1: Force analysis of the sphere in vertical pipe.

When $F_h > 0$, the sphere can go through the vertical pipe, when $F_h = 0$, F_t is called the critical drag, the corresponding fluid velocity is called critical velocity V_t . Hence, when obtaining F_t , Eq.7 can be used to decide whether the sphere can pass vertical pipe or not. The paper uses finite volume simulation method to solve the fluid drag F_t to the sphere in the pipe.

Hypothetically, fluid in the pipe is steady, incompressible and can be treated as Newtonian fluid while going around the sphere. The Re_p exceeds 10^4 with the pipe diameter of above DN200 at economical velocity range pipe flow. Therefore, the fluid flow in the pipe follows the turbulence transportation equation. In order to have a more accurate prediction on the drag force, the standard $k-\omega$ turbulence model is selected [Zaïdi, Fohanno, Taïar and Polidori (2010)] and Fluent 14.0CFD package was used for the calculations. The 3D time-averaged Navier-Stokes (RANS) governing equations are described in the following [Boe, Rodriguez, Plazaola, Banfield, Fong, Casphereero and Vega (2013)]:

Mass conservation:

$$\frac{\partial \rho}{\partial t} + \frac{\partial}{\partial x_i} (\rho u_i) = 0 \quad (8)$$

where ρ is the fluid density, t is the time, u_i is the velocity component along the $x y z$ direction of \mathbf{u} .

Momentum conservation equation:

$$\frac{\partial}{\partial t} (\rho u_i) + \frac{\partial}{\partial x_j} (\rho u_i u_j) = -\frac{\partial p}{\partial x_i} + \frac{\partial}{\partial x_j} \left[\mu \left(\frac{\partial u_i}{\partial x_j} + \frac{\partial u_j}{\partial x_i} - \frac{2}{3} \delta_{ij} \frac{\partial u_l}{\partial x_l} \right) \right] + \frac{\partial}{\partial x_j} \left(-\rho \overline{u'_i u'_j} \right) \quad (9)$$

where p is the pressure on the micro unit of fluid in the pipe, $-\rho\overline{u_i u_j}$ is known as the Reynolds stress tensor, which has to be estimated by a turbulence model to solve the equations above. The Reynolds stress tensor is given by:

$$-\rho\overline{u_i u_j} = \mu_t \left(\frac{\partial u_i}{\partial x_j} + \frac{\partial u_j}{\partial x_i} \right) - \frac{2}{3} \rho k \delta_{ij} \quad (10)$$

where δ_{ij} is the Kronecker delta, which is equal to 1 for $i = j$ and equals to 0 for $i \neq j$, the eddy viscosity μ_t is calculated from:

$$\mu_t = \alpha^* \rho \frac{k}{\omega} \quad (11)$$

where $\alpha^*=1$ with high Reynolds number, k and ω are the kinetic energy and its dissipation rate, which are obtained by solving their conservation equations as given below.

The modeled transport equation for k :

$$\frac{\partial (\rho k)}{\partial t} + \frac{\partial (\rho k u_i)}{\partial x_i} = \frac{\partial}{\partial x_j} \left(\Gamma_k \frac{\partial k}{\partial x_j} \right) + G_k - Y_k \quad (12)$$

The modeled transport equation for ω :

$$\frac{\partial (\rho \omega)}{\partial t} + \frac{\partial (\rho \omega u_i)}{\partial x_i} = \frac{\partial}{\partial x_j} \left[\Gamma_\omega \frac{\partial \omega}{\partial x_j} \right] + G_\omega - Y_\omega \quad (13)$$

where G_k represents the generation of turbulent kinetic energy due to the mean velocity gradients G_ω represents the generation of Γ_ω and Γ_k are the effective diffusivity of k and ω , respectively. Y_k and Y_ω are dissipation of k and ω due to turbulence.

2.2 Solution procedure and boundary conditions

It is not necessary and economical to build a series of real pipe loops to study this problem. A miniature model was built to carry out this research by simulation and experiments. Geometric model and boundary conditions are shown in Fig.2. The diameter of the pipe D is fixed to 40mm. The upper limit of computational domain is L_u and the lower limit L_d .

We used the Grid generation software ANSYS ICEM 14.0 to mesh the geometric models, as shown in Fig.3. The whole computational domain was meshed with a hexahedral-structured grid. Compared with other types of grid, it provides results with higher precision using lower number of grid nodes. Specifically, we subdivided the geometric models using three o-grids, including the mesh refinement for

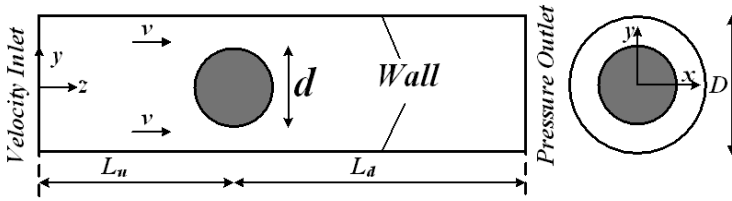


Figure 2: Geometric model and boundary conditions.

the external spherical boundary with one o-grid. The meshes have a good quality of above 0.7.

In this paper, the inlet boundary condition was defined as velocity inlet with vertical direction to the boundary. The average velocity V was chosen between 0.5m/s and 1.5m/s ($Re_p=20000\sim 60000$). The outlet boundary condition was defined as the pressure outlet, the pressure p inside the pipe was set between 0.5Mpa to 1.5Mpa. The outer diameter of the sphere d was equal to 8mm, 12mm, 16mm, 20mm, 24mm, 26mm, 28mm, 30mm, 32mm and 36mm with Re_s ranging from 4000 to 54000 (according to Eq.2). As for other boundary conditions, they can be all defined as the wall boundary conditions, which are default non-slip wall conditions, with a roughness constant of 0.5. Fluid in the pipe is water with density 999.4kg/m^3 and dynamic viscosity 0.001Pas . The flow field changes a lot in pipe wall and the surface of the sphere, so, a finer grid is chosen for these areas, as shown in Fig.3 (b-c). The conservation of mass and momentum equations were solved using the semi-implicit method for pressure-linked equations (SIMPLE) algorithm along with quadratic interpolation for the convective kinematics (QUICK) scheme for convective terms. The computations to obtain the steady velocity and pressure fields were carried out until the residual values of the continuity, x-, y- and z-components of momentum equations decrease to 10^{-6} . The fully converged velocity and pressure fields were further used to evaluate the near-sphere kinematics such as the drag coefficients and streamlines.

2.3 Grid Independence Study

It is mandatory to check numerical artifacts such as upstream/downstream effects and grid independence of the numerical solver. For this purpose, different values of L_u and L_d with diameter ratio $\lambda=0.4$ and 0.8 are examined at $V=0.9\text{m/s}$ and the results are presented in Table 1.

Although all values of upstream and downstream length produce identical results, larger values of $L_u=1.5\text{m}$ and $L_d=4\text{m}$, were chosen.

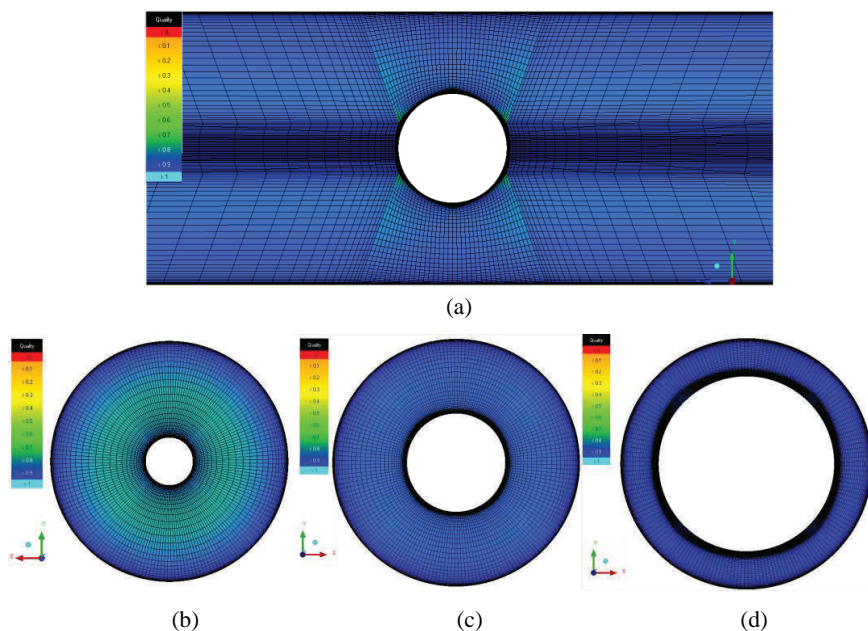


Figure 3: The hexahedral mesh of the sphere inside the pipe. (a) side view at $\lambda=0.4$; (b) front view at $\lambda=0.2$; (c) front view at $\lambda=0.4$; (d) front view at $\lambda=0.7$.

In such bluff body flow systems, the effect of the grid is usually very significant along the surface where fluid is in contact with the solid object. This is because of the possibility of sharp velocity gradients with increasing Reynolds numbers. Therefore, it is mandatory to have a finer grid both on the surface of the sphere and the pipe wall. The drag coefficient results from different mesh schemes simulated at $\lambda=0.4$ and 0.8 are shown in Table 2.

Table 1: Upstream and downstream effects on the Total Drag Coefficients of sphere at $V=0.9\text{m/s}$.

Grid	Total Drag Coefficients(C_D)		
	L_u and L_d	$\lambda=0.4$	$\lambda=0.8$
1	$L_u=1\text{m}$ and $L_d=2\text{m}$	0.6049	2.7864
2	$L_u=2\text{m}$ and $L_d=3\text{m}$	0.6043	2.7861
3	$L_u=1.5\text{m}$ and $L_d=4\text{m}$	0.6047	2.7862

The difference between the drag coefficients at $\lambda=0.4$ achieved using a finer mesh

Table 2: Grid effects on the total Drag Coefficients of sphere at $V=0.9\text{m/s}$ $L_u=1.5\text{m}$ and $L_d=4\text{m}$.

λ	Grid	number of nodes			C_D
		sphere surface	L_u	L_d	
0.4	1	110	30	50	0.6043
	2	144	40	80	0.6047
	3	180	60	100	0.6049
0.8	4	110	30	50	2.7861
	5	144	40	80	2.7862
	6	180	60	100	2.7862

scheme and the relatively coarser version was less than 1%. Using the finer mesh scheme at the higher $\lambda=0.8$ also showed mesh size independence, and the drag coefficient results were within 0.3%. For all average velocity in the pipe, Grid-2 was chosen for $\lambda=0.2\sim 0.5$, and the finer mesh Grid-6 was used for $\lambda=0.6\sim 0.9$.

2.4 Experimental verification methods

In order to verify the simulation method, experimental pipeline platform was built and model spheres of different density and size were designed. Fig.4 is the experimental platform flowchart. In order to observe the movement of the model spheres within the pipe, transparent organic glass was chosen for making the pipes. It has a 5m high vertical segment. The pump's maximum lift was 130m and the flow was $5\text{m}^3/\text{h}$ (1.1m/s). We also put in a needle valve as a flow meter to adjust and display the in-pipe fluid flow velocity at the entrance.

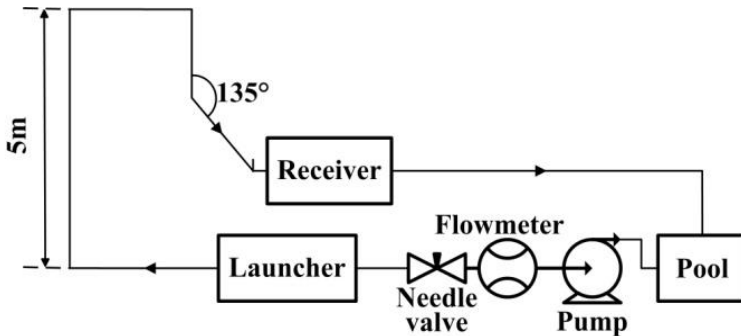


Figure 4: Flowchart of the experimental platform.

The diameter of the pipe used in the simulation model is 40mm. We chose polyoxymethylene (POM) and aluminum (AL) with corresponding density of 1420 kg/m³ and 2700 kg/m³ respectively to make model spheres for this research. Meanwhile, for the purpose of conveniently comparing groups of simulation results with experimental results, different sizes of model spheres were designed which had diameters of 8mm, 16mm, 20mm, 24mm, 30mm and 32mm. Fig. 5 shows the transparent pipeline loop and the model spheres used in the experiments.

Water was flowed into the pipeline using a pump, and then the POM and AL model spheres with different diameters were put into the pipeline using a launcher and were collected at the receiver. We read the critical velocity V_t using the flow meter by adjusting the needle valve to change the water velocity until the sphere floats in the vertical pipe.

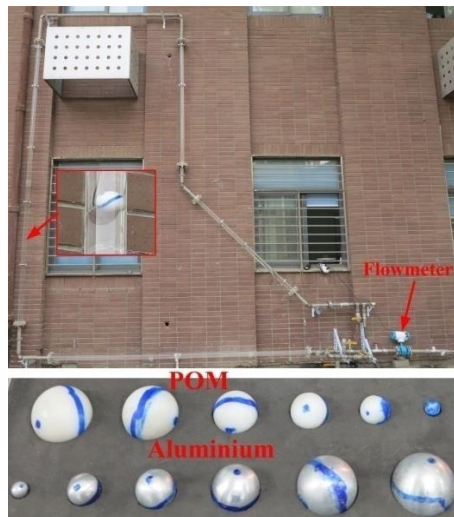


Figure 5: Transparent pipeline loop and the model spheres.

3 Results and discussions

3.1 Pressure and flow behavior around the sphere inside the pipe

Based on the solution procedure and boundary conditions shown in section 2.3, a series of simulations were conducted using the CFD package FLUENT 14.0. More than 60 3-D steady state simulations were carried out and took about 30 minutes for the computation to converge for each case. The computer used in this study had a 16 GB of RAM and an 8 core CPU operating at 3.3GHz.

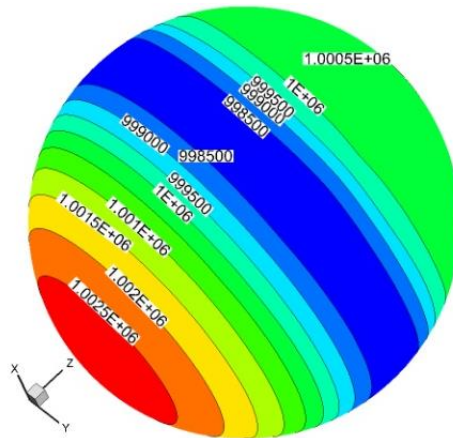


Figure 6: Pressure (pa) contours on the sphere, $V=1\text{m/s}$, $p=1\text{MPa}$, $d=32\text{mm}$.

The pressure contours around the sphere are shown in Fig. 6. It shows that the pressure changes around the sphere are a result of the obstruction to the fluid. The upstream and downstream of the sphere have a pressure difference about 2000 Pa and the pressure distribution on the sphere is spherically symmetric along the flow direction z .

In order to study the factors that influence the pressure distribution on the sphere, the pressure along the semicircle of the sphere at plane $Y=0$ with different line pressure p and velocity V are shown in Fig. 7 and Fig. 8. In order to observe the difference more clearly, the results of the real pressure were subtracted from the line pressure p . It can be seen that there are small changes with the line pressure variation but it changes a lot with the velocity alteration. The area between the curve of pressure and the axes can be seen as the dragon the sphere, so it can be used to deduce that the drag has nothing to do with the line pressure but increases with the velocity in the pipe.

The pressure contours around the sphere at the plane $X=0$ with different sphere diameter are shown in Fig. 9. The line pressure p was set to 1Mpa and the velocity in the pipe $V = 1\text{m/s}$. It can be seen the higher-pressure region of the 32mm sphere is larger than the 16mm one and the pressure difference between upstream and downstream of the sphere is 500Pa for the 16mm sphere and 2000Pa for the 32mm. So it appears that the drag is influenced by the diameter of the sphere or the diameter ratio between the sphere and the pipe.

The velocity contours and streamline with different λ and V at the plane $X=0$ around the sphere are shown in Fig. 10. It is known [Munson, Young, Okiishi

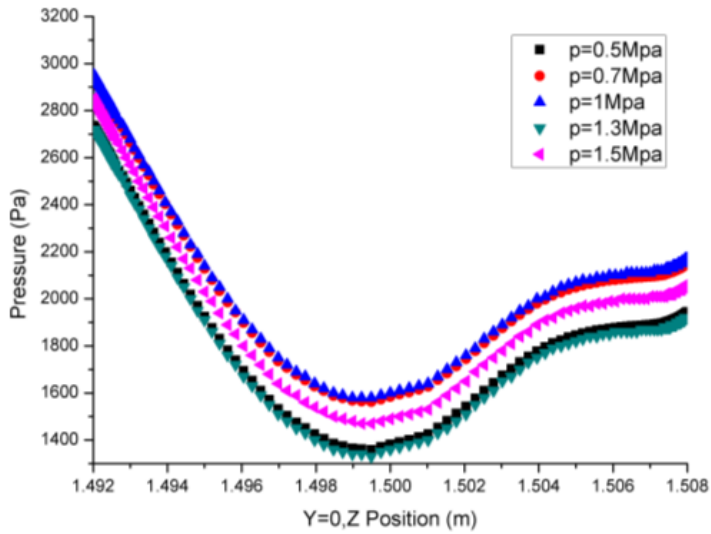


Figure 7: Pressure along the semicircle of the sphere at plane $Y=0$ with different line pressure p , $V=1\text{m/s}$, $d=16\text{mm}$.

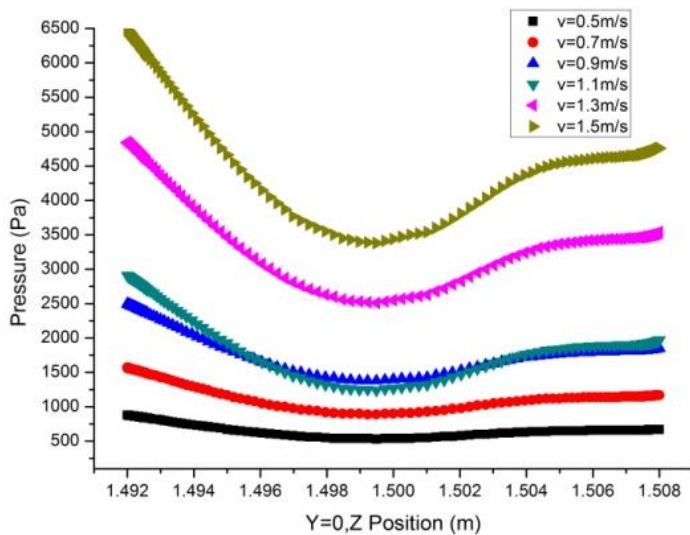


Figure 8: Pressure along the semicircle of the sphere at plane $Y=0$ with different velocity V , $p=1\text{Mpa}$, $d=16\text{mm}$.

and Huebsch (2009); Govardhan and Williamson (2000); Sen, Mittal and Biswas (2012)] that the process of fluid flow around a bluff body (sphere, cylinder) is accompanied by a wake region and boundary layer separation on the downwind side of the body because of the viscous effects.

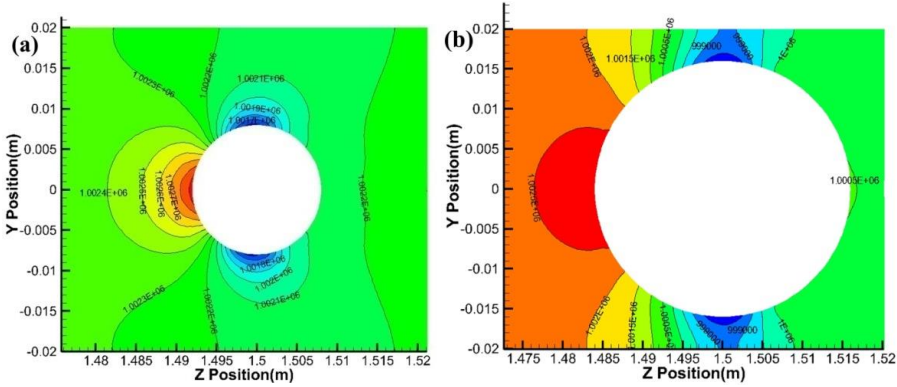


Figure 9: Pressure (pa) contours at the plane $X=0$, close to the sphere, $\lambda=0.4$ for (a) and $\lambda=0.8$ for (b), $V=1\text{m/s}$, $p=1\text{Mpa}$.

For all values of λ and V (except for $\lambda=0.9$ and $V=1.5\text{m/s}$, this is because the Re_s is rather high, the flow behind the sphere becomes unstable, with the wake being very wide and it generates a large amount of drag), two symmetrical steady recirculation wake regions are observed in the rear of the sphere. For $\lambda=0.4$ and 0.6 , the wake region changes a little as the velocity increases from 0.5m/s to 1.5m/s , but if the diameter ratio is larger than 0.6 , it rises a lot as the increasing of V . For fixed V this effect is reinforced as the diameter ratio increased, especially for λ varied from 0.8 to 0.9 . The average pressure on the rear half of the sphere is considerably less than that on the front half because of the boundary layer separation. Thus, a large pressure drag is developed.

3.2 Analyses of the fluid drag on the sphere

The total fluid drag F_t on the sphere along the specified force vector \vec{a} includes the pressure and viscous forces, which is computed by summing the dot product of the pressure and viscosity on each face with the specified force vector:

$$F_t = \left| \vec{a} \cdot \vec{F}_p + \vec{a} \cdot \vec{F}_v \right| \quad (14)$$

Where \vec{a} is the force vector, which is z -axis in this paper, \vec{F}_p is the pressure force vector, \vec{F}_v is the viscous force vector. The pressure force \vec{F}_p is calculated by:

$$\vec{F}_p = \sum_{i=1}^n pA\hat{n} \quad (15)$$

where, n is the number of faces, A is the area of the face, and \hat{n} is the unit normal to the face.

The viscous force \vec{F}_v is computed by:

$$\vec{F}_v = \sum_{i=1}^n f_v A \bar{\tau} \quad (16)$$

where, f_v is the viscous force on the face, and $\bar{\tau}$ is the unit tangential to the face.

The drag on the sphere with different line pressure p was calculated, which indicates that the drag remains a constant as the line pressure changes, which coincides with the results depicted in section 3.1.

The total drag coefficient C_D is defined according to Eq.1 as follows:

$$C_D = \frac{F_t}{\left(\frac{\pi d^2}{4}\right) \left(\frac{1}{2}\rho V^2\right)} = C_{Dp} + C_{Df} \quad (17)$$

where F_t is the drag along the flow direction and C_{Dp} and C_{Df} are pressure and viscous components of the total drag coefficient, respectively. The contributing terms to the drag due to pressure (C_{Dp}) and viscous (C_{Df}) and the total drag coefficient (C_D) are plotted with respect to Re_s for different diameter ratios in Fig. 11. For all values of λ , the total drag coefficient (C_D) decreases with increasing Reynolds number Re_s . For fixed values of Re_s , the overall drag coefficient increases with increasing diameter ratio and the growth is larger as $\lambda \geq 0.6$, and it increases rapidly when λ changes from 0.8 to 0.9, which are in agreement with the discussion in section 3.1. The pressure coefficient plays a major role in the components of the total drag coefficient. This is because at large Reynolds numbers, the contribution of the convection force is larger than the viscous force.

It is more direct and significant to obtain the relationship between the drag (F_t) and diameter ratio (λ), average velocity (V). Fig. 12 plots the total drag on the sphere with different diameter ratio (λ) and different velocity (V). It shows that the drag increases with increasing velocity and diameter ratio. The drag increases little as the λ is less than 0.6, but increases faster as the flow velocity increases when it is larger than 0.65 which is in line with Fig.10 and Fig.12.

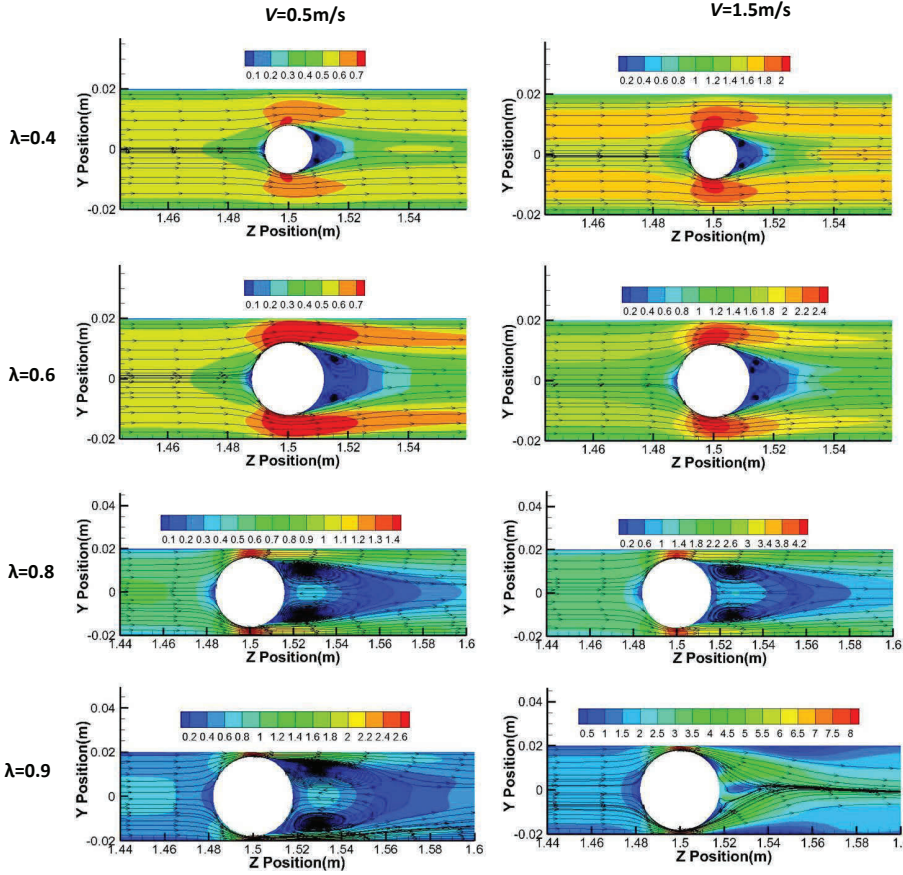


Figure 10: Velocity (m/s) contours and streamline at the plane X=0, close to the sphere V=0.5m/s(left); V=1.5m/s(right).

On the basis of the 48 numerical results, the following empirical formula for the total drag is proposed:

$$F_t = \frac{1.884 - 3.52\lambda - 1.95V^2}{1 + 13.968\ln(\lambda) + 0.016\ln(V) + 0.007V^2}(\lambda V) \quad (18)$$

The above correlation reproduces the simulation data with a root of mean square error of 8% and the coefficient of determination R-square is 0.99947. Fig.13 plots the discrepancies between simulation drag values and those predicted from Eq.18. The above correlation was fit to the CFD data in the range of $0.2 \leq \lambda \leq 0.9$, $4000 \leq Re_s \leq 54000$.

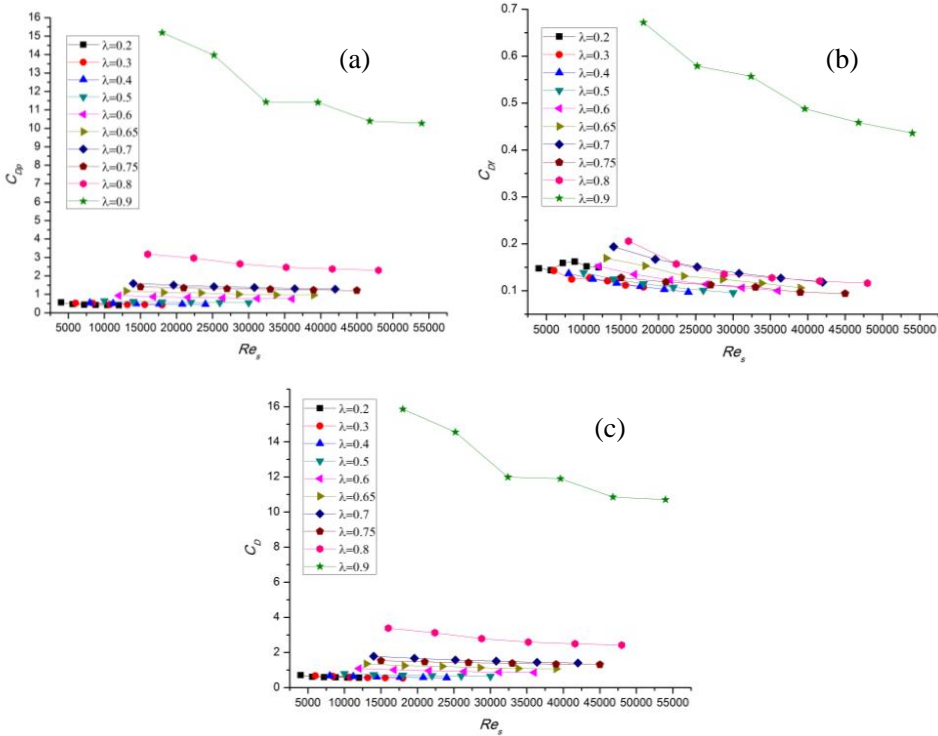


Figure 11: Effects of diameter ratio(λ) on pressure(a) viscous(b) and total drag coefficient (c) variation with Re_s .

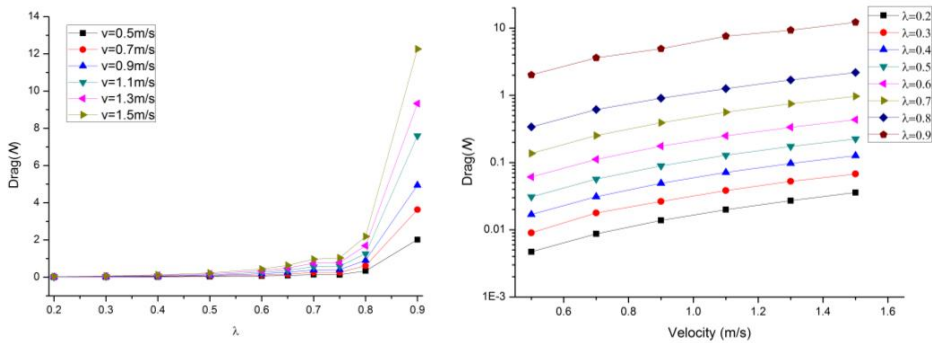


Figure 12: Drag on the sphere with different diameter ratio (λ) and different velocity (V).

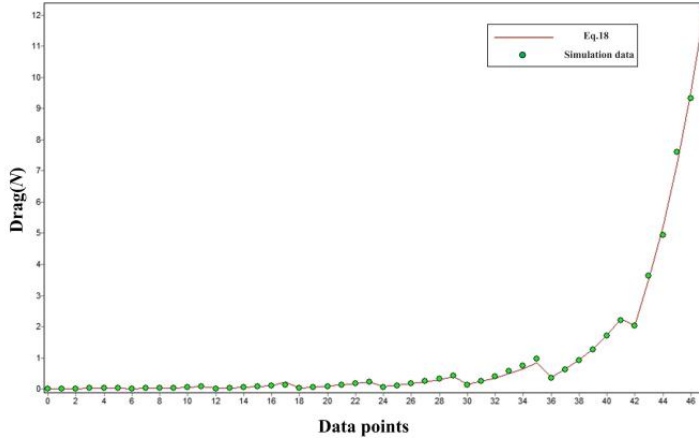


Figure 13: Deviations between the simulation drag and values predicted by Eq.18.

3.3 Experimental results and comparison with simulation

Using the experimental pipeline loop shown in Fig. 5, we leave the spheres suspended in vertical pipe and regulate the needle valve to change water velocity. Then the critical velocity V_t was read through flow meter when the sphere floats in the vertical pipe. The results show that the sphere can pass smoothly when the flow velocity is greater than critical velocity even for a solid steel sphere. Since the density and diameter of the model sphere is known, we can use the results computed in section 3.2 and solve for the critical velocity V_t according to Eq. 7. The results and the error between simulation and experiment are shown in Table. 3. Because of the indication error of the flow meter and the instability caused by the pump when adjusting the pressure, there must be error in the critical velocity. We can see that for larger λ , the error becomes increases, which may be related to the vibration of the sphere due to the vortex mentioned in section 3.1. The experimental results show that for larger λ is the sphere floats violently in the pipe. The maximum error is 3.1%, which is acceptable in this particular application

3.4 Analyses of the passing ability of the spherical leak detector in the real pipeline

The prototype of the spherical inner detector has a pressure proof aluminum shell, which is coated by a layer of polyurethane foam. The detector is equipped with batteries, a data acquisition device, magnetic sensor acoustic sensor and data storage device. The outer diameter is 184mm and the average density of this whole sphere is 1300kg/m^3 . We want to make sure that at which flow velocity and pipe diameter

Table 3: Critical speed and the error between simulation and experiment.

λ	POM			AL		
	V_t (m/s)		Error (%)	V_t (m/s)		Error (%)
	Expt.	Sim.		Expt.	Sim.	
0.2	0.224	0.228	1.7	0.500	0.508	1.6
0.4	0.328	0.333	1.5	0.738	0.747	1.2
0.5	0.359	0.351	2.2	0.787	0.797	1.2
0.6	0.324	0.329	1.5	0.749	0.757	1.1
0.75	0.226	0.231	2.2	0.518	0.529	2.1
0.8	0.189	0.195	3.1	0.414	0.424	2.4

the detector can pass through the vertical segment of the pipeline.

Because the 184mm sphere is moving in the pipe flow at velocity of 0.5m/s~1.5m/s, it exceeds the Re_s range in Eq.18. Due to this the drag on the sphere could not to be calculated according to Eq.18, but the simulation method was verified by comparing with the experimental critical velocity in section 3.3 and we believe it is receivable. Using the simulation method discussed above, more than 66 numerical simulations were conducted with pipe diameter D ranging from 8~28 inches and flow velocity ranging from 0.7m/s~1.2m/s. The resultant force on the spherical inner detector in vertical segment of the pipeline is solved using Eq.7. The results are shown in Fig. 14.

It can be seen that when the pipe diameter is constant, the resultant force grows larger with increase inflow velocity. However, the drag barely increases with flow velocity when the diameter is larger than 10-inch, and the resultant force is less than zero illustrating that it could not go through the vertical pipe. When the pipe diameters are 10 or 8inch, that is, the diameter ratio reaches 73%; the resultant force significantly increases and grows with the flow velocity.

Using the prototype of the spherical inner detector, a passing ability test was carried out at a 150m long and diameter of 200mmpipe loop shown in Fig.15. The results show that the detector could get to the receiving trap smoothly if the pipe flow reaches 80m³/h (0.7m/s), the resultant force at this condition is 67N (simulation data) and is sufficient for pass through the vertical pipe smoothly. But if the pipe flow decreases to 56m³/h (0.5m/s resultant force=40N), the detector was not able to reach the receiving trap it is observed that the detector could go through the vertical segment but it is obstructed at the bend on the top, because of the bend's reactive force to the detector. This is another complex problem that needs to be

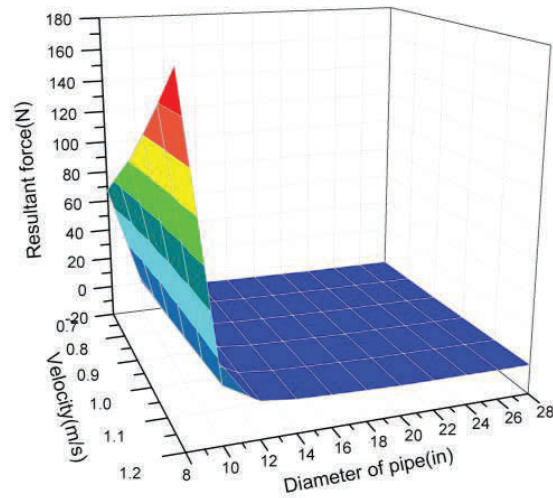


Figure 14: 3D surface of resultant force with different velocity and pipe diameter.



Figure 15: Test pipeline loop, sphere receiving (left), 1.5m high vertical pipe (right).

studied for the hydrodynamic force acting on the sphere at the bend. However, we know that the prototype of the spherical detector can go through within normal economical flow velocity (0.7m/s-1.5m/s) in 8 or 10-inch pipelines based on the results of the simulation method discussed above. We believe it is a good choice when λ ranges from 0.7~0.8, because the drag on sphere rises signally and is not too large to be obstructed at the bend if λ is in this range One can select the λ

in this range and balance this parameter according to the F_f , F_t and G during the design stage for different pipe sizes.

4 Conclusions

In this paper, finite volume simulation and experiments were carried out to explore the passing ability of the spherical leak detector inside the vertical segment of the pipe. For sphere with different sizes and density, different flow rate, more than 100 3-D steady numerical simulation analysis and experiments with the same parameter were carried out. The simulation shows that the drag on the sphere by the flow inside the pipe is related to the flow velocity V and the diameter ratio λ . The drag increase little as λ is less than 0.6, but grows faster as the flow velocity increases when λ is larger than 0.65. An empirical formula for the total drag with λ and V is established here for $0.2 \leq \lambda \leq 0.9$, $4000 \leq Re_s \leq 54000$, and the correlation reproduces the simulation data with a root of mean square error of 8% and the coefficient of determination R-square is 0.99947. The simulation data was verified by comparing the experimental critical velocity when the sphere floats in the pipe with the data for the simulation. The results indicate that the simulation and the experimental results agree with each other. Finally, the passing ability of the sample detector with diameter of 184mm and average density of 1300 kg/m^3 in 8-28 inch pipeline is predicted using this method, it shows that the sample spherical detector could go through within normal economical flow velocity (0.7m/s-1.5m/s) in 8 or 10-inch pipelines. A passing ability test of the sample detector was carried out in a pipe loop and the results were line with the simulation results. We believe it is a good choice for λ ranging from 0.7~0.8 based on the above analysis.

Acknowledgement: This study is funded by National Natural Science Foundation of China (51004076 and 61473205) and Tianjin Research Program of Application Foundation and Advanced Technology (14JCQNJC04900).

References

- Bockler, W.** (2012): Reliable and Cost Effective Leak Detection with an New Generation of Ultrasonic Pigs. *In 7th Pipeline Technology Conference*, Hannover, Germany.
- Boe, C.; Rodriguez, J.; Plazaola, C.; Banfield, I.; Fong, A.; Casphereero, R.; Vega, A.** (2013): A Hydrodynamic Assessment of a Remotely Operated Underwater Vehicle Based On Computational Fluid Dynamic - Part 1-Numerical Simulation. *CMES-Computer Modeling in Engineering & Sciences*, vol. 90, no. 2, pp. 165-77.
- Chhabra, R. P.; Kumar, M.; Prasad, R.** (2000): Drag On Spheres in Rolling

Motion in Inclined Smooth Tubes Filled with Incompressible Liquids. *Powder Technology*, vol. 113, no. 1, pp. 114-18.

Fletcher, R.; Chandrasekaran, M. (2009): Smartsphere-A New Approach in Pipeline Leak Detection. In *Proceedings of the Biennial International Pipeline Conference*, Calgary, Canada.

Fuchs, H. V.; Riehle, R. (1991): Ten Years of Experience with Leak Detection by Acoustic Signal Analysis. *Applied Acoustics*, vol. 33, no. 1, pp. 1-19.

Gloria, N. B. S.; Areiza, M. C. L.; Miranda, I. V. J.; Rebello, J. M. A. (2009): Development of a Magnetic Sensor for Detection and Sizing of Internal Pipeline Corrosion Defects. *NDT&E International*, vol. 42, no. 8, pp. 669-77.

Govardhan, R.; Williamson, C. (2000): Modes of Vortex Formation and Frequency Response of a Freely Vibrating Cylinder. *Journal of Fluid Mechanics*, vol. 420, pp. 85-130.

Hasan, M. A. (1986): Wall Effects On the Motion of a Rolling Sphere in a Closely Fitting Tube. *The Chemical Engineering Journal*, vol. 33, no. 2, pp. 97-101.

Jalaal, M.; Ganji, D. D. (2011): On Unsteady Rolling Motion of Spheres in Inclined Tubes Filled with Incompressible Newtonian Fluids. *Advanced Powder Technology*, vol. 22, no. 1, pp. 58-67.

Krishnan, S.; Kannan, A. (2010): Effect of Blockage Ratio On Drag and Heat Transfer From a Centrally Located Sphere in Pipe Flow. *Engineering Applications of Computational Fluid Mechanics*, vol. 4, no. 3, pp. 396-414.

Lee, S. H.; Wu, T. (2007): Drag Force on a Sphere Moving in Low-Reynolds-Number Pipe Flows. *Journal of Mechanics*, vol.23, no.4, pp.423-32.

Lei, H.; Huang, Z.; Liang, W.; Mao, Y.; Que, P. W. (2009): Ultrasonic Pig for Submarine Oil Pipeline Corrosion Inspection. *Russian Journal of Nondestructive Testing*, vol. 45, no. 4, pp. 285-91.

Li, B.; Chen, S.; Zhao, W.; Guo, S.; Liu, Y. (2012): Research On Tiny Leak System for Oil Transmission Pipelines. In *Proceedings of the 2012 International Conference on Computer Distributed Control and Intelligent Environmental Monitoring*, Hunan, China.

Lopez, J. M.; Sadovnychiy, S. (2007): Small PIG for Inspection Pipeline. In *Electronics, Robotics and Automotive Mechanics Conference, CERMA 2007 - Proceedings*, Morelos, Mexico.

Munson, B. R.; Young, D. F.; Okiishi, T. H.; Huebsch, W. W.(2009): Fundamentals. of. Fluid. Mechanics. Wiley-Blackwell, USA.

Quarini, I.; Shire, S. (2007): A Review of Fluid-Driven Pipeline Pigs and their Applications. *Journal of Process Mechanical Engineering*, vol. 221, no. 1, pp.

1-10.

Rajasekhar Reddy, C.; Kishore, N. (2012): Wall Retardation Effects on Flow and Drag Phenomena of Confined Spherical Particles in Shear-Thickening Fluids. *Industrial & Engineering Chemistry Research*, vol. 51, no. 51, pp. 16755-62.

Sen, S.; Mittal, S.; Biswas, G. (2012): Steady Separated Flow Past Elliptic Cylinders Using a Stabilized Finite-Element Method. *CMES-Computer Modeling in Engineering & Sciences*, vol. 86, no. 1, pp. 1-27.

Song, D.; Gupta, R. K.; Chhabra, R. P. (2009): Wall Effects on a Sphere Falling in Quiescent Power Law Fluids in Cylindrical Tubes. *Industrial & Engineering Chemistry Research*, vol. 48, no. 12, pp. 5845-56.

Tang, H. (2007): Determination of Economical Flowing Velocity of Product Oil in Pipeline. *Petroleum Planning & Engineering*, vol. 18, no. 2, pp. 33-34.

Tian, C.; Yan, J.; Huang, J.; Wang, Y.; Kim, D.; Yi, T. (2012): Negative Pressure Wave based Pipeline Leak Detection: Challenges and Algorithms. In *2012 IEEE International Conference on Service Operations and Logistics and Informatics*, Suzhou, China.

Zaidi, H.; Fohanno, S.; Taiar, R.; Polidori, G. (2010): Turbulence Model Choice for the Calculation of Drag Forces When Using the CFD Method. *Journal of Biomechanics*, vol. 43, no. 3, pp. 405-11.

Zhou, Y.; Yin, L. (2012): Self-Detection of Leaking Pipes by One-Dimensional Photonic Crystals. *Chinese Physics Letters*, vol. 29, no. 6, pp. 64213.